Effect of Inverse Solutions, Connectivity Measures, and Node Sizes on EEG Source Network: A Simultaneous EEG Study

Yang Liu, Heng Su, and Chunsheng Li, *Member, IEEE*

Abstract— **Brain network provides an essential perspective for studying normal and pathological brain activities. Reconstructing the brain network in the source space becomes more needed, for example, as a target in non-invasive neuromodulation. Precise estimating source activities from the scalp EEG is still challenging because it is an ill-posed question and because of the volume conduction effect. There is no consensus on how to reconstruct the EEG source network. This study uses simultaneous scalp EEG and stereo-EEG to investigate the effect of inverse solutions, connectivity measures, and node sizes on the reconstruction of the source network. We evaluated the performance of different methods on both source activity and network. Numerical simulation was also carried out for comparison. The weighted phase-lag index (wPLI) method achieved significantly better performance on the reconstructed networks in source space than five other connectivity measures (directed transfer function (DTF), partial directed coherence (PDC), efficient effective connectivity (EEC), Pearson correlation coefficient (PCC), and amplitude envelope correlation (AEC)). There is no significant difference between the inverse solutions (standardized low-resolution brain electromagnetic tomography (sLORETA), weighted minimum norm estimate (wMNE), and linearly constrained minimum variance (LCMV) beamforming) on the reconstructed source networks. The source network based on signal phases can fit intracranial activities better than signal waveform properties or causality. Our study provides a basis for reconstructing source space networks from scalp EEG, especially for future neuromodulation research.**

Index Terms— **EEG source network, simultaneous EEG, EEG source imaging, connectivity measure, node size.**

I. Introduction

BRAIN network dysfunction or abnormalities have been implicated in various neurological disorders, such as epilepsy, Parkinson's disease, stroke, and others [1], [2], [3]. Brain network analysis offers crucial assistance in diagnosing and treating these conditions [4], [5], [6]. Non-invasive functional neuroimaging techniques have significantly enhanced our comprehension of brain networks, offering insights into both normal and pathological brain states. Non-invasive neuromodulation techniques, such as transcranial magnetic stimulation(TMS) [7], transcranial direct current stimulation (tDCS) [8], and transcranial focused ultrasound stimulation (tFUS) [9], have been widely investigated in treating brain diseases [10], [11]. The reconstruction and analysis of individualized brain networks may significantly improve the therapeutic effect. Electroencephalogram (EEG) is an ideal tool for feedback of transcranial stimulation because of its high temporal resolution. Still, it falls short in estimating the brain network underneath the skull due to the volume conduction effect. The EEG source imaging (ESI) may solve this problem by considering the volume conduction effect and physiological or anatomical constraints in inverse solution [12], [13], [14]. From the perspective of EEG source connectivity, there is still no consensus on solving the inverse solution and which network measure provides a better reconstructed network in source space.

ESI methods have been widely used in scalp EEG analysis, including standardized low-resolution brain electromagnetic tomography (sLORETA) [15], weighted minimum norm estimate (wMNE) [16], and linearly constrained minimum variance (LCMV) [17] beamforming, ESI has played an essential role in the localization of epileptic lesions [18], [19], [20]. Recently, some studies adopted machine learning approaches to solve the inverse solution [21], [22], [23]. Source leakage may blur the EEG source network [24]. Some studies have investigated the effect of channel density, inverse solutions, connectivity measures, and source extraction measures on EEG source networks [25], [26], [27], [28]. While no ground truth is available in most cases, numerical simulation is widely used in investigating EEG source networks [29], [30]. Simultaneous scalp EEG and intracranial EEG provide the best model for studying EEG source networks because the intracranial activities can be treated as the ground truth of the scalp EEG's inverse solution [31], [32], [33]. To our knowledge, rare studies use simultaneous intracranial EEG recording for evaluating the source network reconstruction measures.
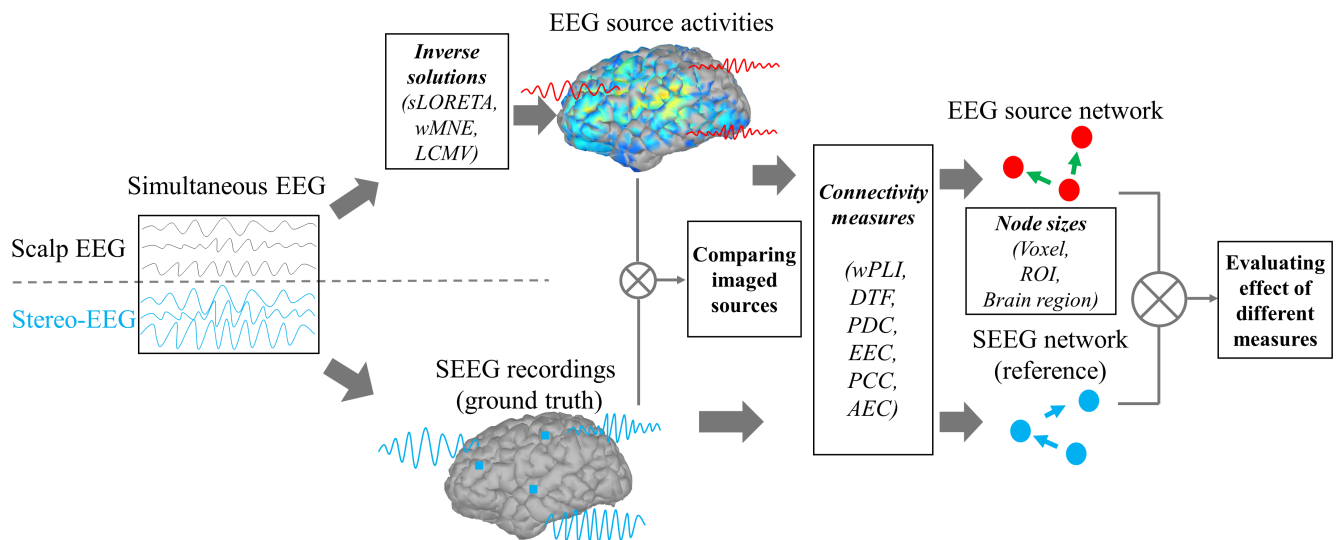
Fig. 1. The workflow for evaluating the effect of inverse solutions, connectivity measures, and node sizes on EEG source network using simultaneous EEG. Three inverse solutions, six connectivity measures, and three node sizes were investigated. The Pearson correlation between the EEG source network and the SEEG network was calculated to evaluate the performance of the different approaches.

In this study, we investigated the effect of three inverse solutions, six connectivity measures, and three node sizes of the EEG source network on a simultaneous EEG recording dataset, including: (1) three inverse solutions: sLORETA, wMNE, and LCMV. (2) six connectivity measures: the directed transfer function (DTF), partial directed coherence (PDC), efficient effective connectivity (EEC), weighted phase lag index (wPLI), Pearson correlation coefficient (PCC), and amplitude envelope correlation (AEC). (3) three node sizes: voxels, regions of interest (ROIs) [34], [35], and brain regions [26], [36]. The workflow of this study is shown in Fig. 1.

II. MATERIALS AND METHODS

A. Data and Preprocessing

The simultaneous scalp EEG and Stereo-EEG (SEEG) analyzed in this study is part of the "Open Science Framework" (https://doi.org/10.17605/OSF.IO/WSGZP) [37]. Subjects enrolled in the study had drug-resistant epilepsy and met the criteria for surgical resection. Data collection took place during interictal periods between the patients' epileptic seizures. Single-pulse electrical stimulation was administered to non-epileptic regions of the brain. The SEEG data were recorded through a 192-channel recording system and 256-channel high-density scalp electrodes. We used the averaged evoked potentials for each trail, and the SEEG signals only from contacts on the cortex were used. The duration of each averaged signal following stimulation is 700 ms. The simultaneous EEG were filtered at 1-45 Hz.

The SEEG was recorded in only parts of the brain for a given patient, and there might be some scalp EEG activities unrelated to the simultaneous SEEG activities. To minimize the effect of unknown sources on our analysis, we chose the EEG data to mostly represent the underneath SEEG activities. All trails of SEEG recordings were forward-project onto the scalp using individual head models, and we calculated the

correlations between the SEEG forward-projected signal and the scalp EEG. The simultaneous EEG trials with correlation in the top 5% were chosen, and the correlation values are all above 0.7. It resulted in 13 trials from ten patients (sub01-02, sub03-03, sub13-01, sub14-01, sub14-08, sub16-02, sub18-02, sub18-05, sub18-08, sub22-10, sub23-05, sub32-04, sub35-09). The ten patients had 179 SEEG contacts. We mapped those contacts from individual head models to a standard Montreal Neurological Institute (MNI) head model, as shown in Fig. 2.

Individual T1-weighted brain magnetic resonance imaging (MRI) generated the patient-specific head models, which were used in ESI. The Brainstorm toolbox, along with Brainsuite and SVReg [38], [39], [40], was used to process the head models. The cerebral cortex is subsequently divided into 66 distinct brain regions. A three-layer head model comprising scalp, skull, and brain tissue was constructed using the boundary element method (BEM). The assigned conductivities for these layers are 1.00 S/m, 0.0125 S/m, and 1.00 S/m, respectively [34], [41].

B. Workflow for Evaluating the Effect

The simultaneous scalp EEG and SEEG were used for evaluation, as shown in Fig. 1. The SEEG signal was treated as the ground truth of the scalp EEG's inverse solution. First, the scalp EEG was imaged to source activities using ESI measures. The EEG source activities were compared with the SEEG recordings. Then, the EEG source network was obtained using connectivity measures. The SEEG network was used as the reference for evaluating the EEG source network for a given connectivity measure. The similarity between the EEG source networks and the SEEG networks was calculated by Pearson correlation. The performance of different measures is evaluated based on correlation value. The higher the correlation value, the better the ESI-connectivity approach.
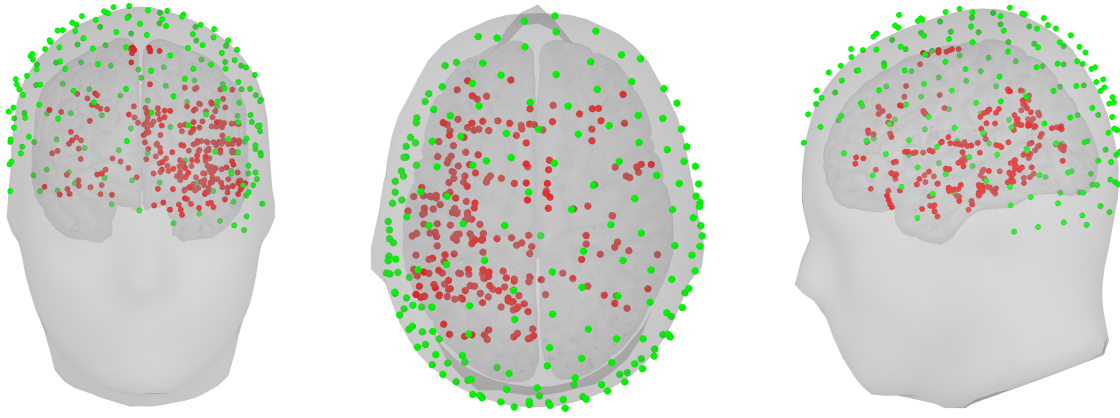
Fig. 2. The distribution of SEEG contacts and scalp electrodes on the standard MNI head model. The red and green dots represent SEEG contacts and scalp electrodes, respectively.

The correlation is referred to as the Pearson correlation in this study.

C. Inverse Solutions

The inverse problem of source imaging involves inferring underlying source activity from recorded brain activity. The electrical potentials recorded on the scalp sensors can be obtained by the following [30]:

$$U = LJ + N \qquad (1)$$

where U is the recorded potential vector located at the scalp electrode. L is the lead field. J is the current density vector at each voxel position, and N is the noise. Given that the known quantities in source imaging are significantly fewer than the unknown quantities, the study of inverse problems necessitates using prior information to impose constraints. We use sLORETA, wMNE, and LCMV to estimate the value of the estimated current density of voxels ($\hat{J}$).

1) sLORETA: sLORETA estimates the current density using the minimum norm solution. The standardized estimated current density is used to infer the location of intracranial sources [15]. The value of $\hat{J}$ is the following:

$$\hat{J} = TU \qquad (2)$$

where $T = L^T[LL^T + \lambda H]^+$ with $H = I - 11^T/1^T1$, H denotes the centering matrix, I is the identity matrix, 1 is a vector of ones, λ is the regularization parameter, and $[\cdot]^+$ denotes Moore-Penrose pseudoinverse. To obtain the standardized $\hat{J}$, it is imperative to determine its variance ($S_{\hat{j}}$).

$$S_{\hat{j}} = L^T[LL^T + \lambda H]^+ L \qquad (3)$$
$$\hat{J} = S_{\hat{j}} J \qquad (4)$$

2) wMNE: The wMNE compensates for the depth dependency of the standard solution of the minimum norm least squares by weighting the source current components [16]:

$$minimize\ \Delta = \left\| U - L\hat{J} \right\|_2^2 + \lambda \left\| C\hat{J} \right\|_2^2 \qquad (5)$$
$$\hat{J} = (C^TC)^{-1}L^T(L(C^TC)^{-1}L^T + 1\lambda)^{-1}U \quad (6)$$

where C is the weighting matrix related to the number of dipoles and their components. C can be calculated using the singular value decomposition.

3) LCMV: In this study, we employed the LCMV method in the Brainstorm toolbox, where the noise covariance matrix is substituted with its inverse, commonly known as dipole modeling [38].

D. Connectivity Measures

1) DTF: A causal network enables the quantification of directed connectivity among network nodes. This study employs the DTF to characterize the information intensity and the transmission directionality between brain network nodes. The DTF is based on the autoregressive (AR) model, which is as follows:

$$x_t = \sum_{r=1}^{p} A_r x_{t-r} + e_t \qquad (7)$$

where p is the model order, x_t denotes the state vectors of EEG, e_t is the vector of the white noise process, and A_r are the coefficient matrices, which can be obtained by multiplying both sides by x_{t-s}^T. By applying the z-transform, we get the transfer function of the AR model:

$$H(f) = \left(I - \sum_{r=1}^{p} A_r e^{-i2\pi f r \Delta t} \right)^{-1} \qquad (8)$$

where I is the identity matrix. f is frequency. Δt is the sampling interval. Performing row normalization on $H(f)$ such that the contribution of all channels to the ith channel is equal to 1, the causal relationship between the measurement channels is calculated:

$$\gamma_{ij}^2 = \frac{\left| H_{ij}(f) \right|^2}{\sum_{m=1}^{k} |H_{im}(f)|^2} \qquad (9)$$

In this study, surrogate analyses [42] were performed 1000 times, and the causal values exceeding the top 5% were selected for subsequent analysis.

2) PDC: Partial directed coherence (PDC) analyzes the connectivity between multi-channel signals, which is also based on Granger causality [43]. Contrasting with DTF, PDC measures the direct connectivity between two nodes, excluding contributions from other nodes. Similarly, surrogate analyses were performed 1000 times.

3) EEC: EEC is considered to provide a better estimation of directed causal relationships [44], enabling more effective identification of node connections. The AR model and the Brug method are employed to calculate the spectrum shown in the following:

$$P(\omega) = \frac{\sigma^2 T_s}{\left| 1 + \sum_{l=1}^{p} a_l \exp(-il\omega T_s) \right|^2} \tag{10}$$

where, ω represents the angular frequency, T_s is the sampling period, σ^2 denotes the power of the noise, and a_l refers to the parameters of the p-order AR model [44].

The sum of maximum connectivity is used for normalization. The threshold is dynamic. Spectral values exceeding it are retained, while those falling below are assigned a value of 0.

4) wPLI: The wPLI measures the degree of phase synchronization between two signals by weighting the cross-spectrum of their phases [45]. It is calculated as follows:

$$wPLI = \frac{|E\{|\Im\{X\}|sgn(\Im\{X\})\}|}{E\{|\Im\{X\}|\}} = \frac{|E\{\Im\{X\}\}|}{E\{|\Im\{X\}|\}} \tag{11}$$

Here, $|\cdot|$ denotes the absolute value. $E\{\cdot\}$ denotes the mathematical expectation calculator. $sgn()$ is the sign function. $\Im\{X\}$ corresponds to the imaginary part of the cross-spectrum. The Hilbert transform applied to the signals obtains the instantaneous phase angle.

5) PCC: The Pearson correlation coefficient (PCC) quantifies the linear correlation between channels in the EEG signal. It measures the extent of linear correlation between two variables, as shown in the following:

$$P_{a,b} = \frac{\text{cov}(a, b)}{\sigma_a \sigma_b} \tag{12}$$

where $P_{a,b}$ denotes the degree of linear correlation between n dimensional signals a and b. $cov(a, b)$ denotes the covariance between variables a and b, and σ_a, σ_b denote the standard deviation of a and b, respectively.

6) AEC: The AEC of the signal, derived from the Hilbert transform, indicates the synchrony among different brain regions [26].

E. Node Sizes

Node size is one factor influencing EEG source connectivity. This study separately selects the voxels, ROIs, and brain regions as network nodes. The voxels represent the smallest unit within the head model. Specifically, the BEM head model in this research comprises a cortex model of 15,000 voxels. To compare the reconstructed network with the SEEG network, the voxels closest to the SEEG contacts were selected for analysis. In this study, the ROI was fixed to a circle with a radius of 12.5 mm [30], and the voxels closest to the SEEG

contacts were the center of the ROI. The brain regions with SEEG contacts are used as nodes when analyzing the network between brain regions. The connectivity between ROIs or brain regions containing multiple voxel points is extracted using the *mean-after* approach [27].

F. Numerical Simulation

We also investigated the source network with simulated data to compare it with the result of the simultaneous EEG. Based on the lead matrices, the simulated intracranial sources were first forward-projected on the scalp. ESI methods solved the source activities for those projected signals. To evaluate the performance, the source connectivities reconstructed from the simulated and imaged sources were compared. This procedure is similar to the analysis of simultaneous EEG recording, except that simulated intracranial sources forward-project to fake scalp EEG.

The SEEG contacts used in this study mainly reside in the frontal, temporal, and parietal lobes. The simulated sources were randomly placed perpendicular to the cortical surface in a brain region, a randomly selected one of the above three brain lobes. Each brain region contains three simulated sources. Equation (13) is the mathematical model with nine simulated nodes.

$$
\begin{cases}
Z_{11}(t) = \Phi(t) + n_{11}(t) \\
Z_{12}(t) = 0.2Z_{11}(t - 0.2) + 0.2Z_{12}(t - 0.1) + n_{12}(t) \\
Z_{13}(t) = 0.15Z_{11}(t - 0.2) + 0.1Z_{13}(t - 0.1) + n_{13}(t) \\
Z_{21}(t) = 0.35Z_{11}(t - 0.1) + 0.25Z_{21}(t - 0.0075) \\
\qquad\qquad + 0.1Z_{21}(t - 0.0125) + n_{21}(t) \\
Z_{22}(t) = 0.3Z_{21}(t - 0.2) + 0.125Z_{22}(t - 0.2) + n_{22}(t) \\
Z_{23}(t) = 0.1Z_{21}(t - 0.2) + 0.3Z_{23}(t - 0.1) + n_{23}(t) \\
Z_{31}(t) = 0.6Z_{11}(t - 0.2 + 0.1Z_{31}(t - 0.0125) + n_{31}(t) \\
Z_{32}(t) = 0.4Z_{31}(t - 0.2) + 0.3Z_{32}(t - 0.2) + n_{32}(t) \\
Z_{33}(t) = 0.2Z_{31}(t - 0.2) + 0.1Z_{33}(t - 0.1) + n_{33}(t)
\end{cases}
\tag{13}
$$

where Z_{i1} (i = 1, 2, 3) represents the simulated source in the ith brain region. The Φ is a simulated Gauss signal. The n_{ij} is a white noise signal added on Z_{ij} (i = 1, 2, 3 and j = 1, 2, 3). The Z_{21} and the Z_{31} are affected by the Z_{11} with a delay.

We used the network with nine nodes since its size is closer to the SEEG network [30]. The candidate regions for the location of the nodes are shown in Fig. 3(a). The simulated source signals and connectivity diagram for nine nodes are shown in Fig. 3(b).

G. Statistical Analysis

We employed the Wilcoxon signed-sum test to compare differences between paired samples with significance level is 0.01. The Wilcoxon rank-sum test was used to compare differences in samples from five unpaired sets of lobes. The false discovery rate (FDR) is used for multiple statistical corrections.

III. RESULT

We present the results with simulated data and simultaneous EEG separately.

A. Simulated Data

Fig. 3(c)-3(e) shows the correlations between the simulated and the imaged sources. There are no significant differences between the three inverse solutions at the voxel level. At the ROI level, LCMV is higher than sLORETA (p < 0.01) and wMNE (p < 0.01). At the region level, wMNE is higher than sLORETA (p < 0.01).

The correlations between the simulated network and imaged source network using three inverse solutions with six connectivity measures were shown in Fig. 3(f)-(h) and Table I. The wPLI is significantly higher than the other five connectivity measures ($p < 0.01$). AEC is also higher than DTF ($p < 0.01$), PDC ($p < 0.01$) and PCC ($p < 0.01$). No significant difference was found between EEC and AEC ($p = 0.09$). EEC is higher than DTF ($p < 0.01$) and PDC ($p < 0.01$). DTF is also higher than PDC ($p < 0.01$).

B. Simultaneous EEG

1) EEG Source Imaging: The correlations between the imaged sources and the SEEG recordings are shown in Fig. 4(a)-4(c). There are no significant differences between the three inverse solutions at the voxel, ROI, or region level. We divided the SEEG contacts into five groups: frontal lobe, temporal lobe, parietal lobe, occipital lobe, and cingulate cortex. At the voxel level, the correlation between the imaged sources and the SEEG signals of the five groups is shown in Fig. 4(d)-4(f). When sLORETA was used, the correlation at the frontal lobe was higher than that at the temporal lobe ($p = 0.01$), the parietal lobe ($p = 0.03$), the occipital lobe ($p = 0.44$), and the cingulate cortex($p = 0.14$). When wMNE was used, the correlation at the frontal lobe was higher than that at the temporal lobe ($p = 0.01$), the parietal lobe ($p = 0.02$), the occipital lobe ($p = 0.54$), and the cingulate cortex($p = 0.17$). When LCMV was used, the correlation at the parietal lobe was higher than that at the other four groups but without significance, which differs from the sLORETA and wMNE.

2) EEG Source Network: The correlation between the EEG source network and SEEG network using six connectivity measures is shown in Fig. 5. The wPLI is significantly higher than the other five connectivity measures ($p < 0.01$), and the median values of correlation are shown in Table II. AEC is higher than DTF ($p < 0.01$) and PCC ($p < 0.01$). The DTF performed similarly to the EEC. Both the correlations of DTF and EEC are higher than the PDC for all three inverse solutions. DTF is higher than PCC ($p < 0.01$). The wPLI scored the highest similarity between the EEG source network and the SEEG network; EEC, AEC, and DTF followed. The PCC scored the lowest similarity.

When we consider the wPLI network only, the correlation using LCMV is higher than that using sLORETA ($p = 0.71$) and wMNE ($p = 0.64$). The wMNE/wPLI and sLORETA/wPLI at the voxel level performed equally well,

as shown in Table II. While at the ROI and brain level, LCMV/wPLI is higher than wMNE/wPLI.

3) Scalp EEG Network: We investigated whether the EEG source network performs better than the scalp EEG network without using ESI. The above two networks were compared to the SEEG network to evaluate their performance. Here, scalp EEG electrodes nearest to the underneath SEEG contacts were chosen as the nodes of the scalp EEG network. The correlations between the SEEG network and the network with or without ESI are shown in Fig. 6. The correlation of the scalp EEG network without using ESI is lower than that of the source network by sLORETA ($p = 0.02$), wMNE ($p = 0.06$) or LCMV ($p = 0.007$).

IV. DISCUSSION

A. Effect of Connectivity Measures

This study uses simultaneous scalp EEG and SEEG to validate the reconstructed brain network in the source space. The main difference from the numerical simulation is that the SEEG signal provides the ground truth for the EEG imaged sources. In our simultaneous EEG analysis, the wPLI reconstructs the network with a significantly higher correlation than DTF, PDC, EEC, PCC, and AEC measures. The wPLI was proposed as a functional connection measure to solve source leakage in ESI [45]. The phase of intracranial activities could be better recovered by ESIs, as suggested by some other studies [26], [46]. When wPLI was used as a connectivity measure, there were no significant differences between the three inverse solutions. However, the correlation of LCMV was higher than wMNE and sLORETA (Table II).

AEC and PCC are both using time-domain features. The performance of AEC is better than that of PCC (Table I and Table II), which suggests that the signal's envelope is more robust than the waveform for reconstructing source connectivity. DTF, PDC and EEC are based on the causality between nodes. The low performance of these three measures suggests that volume conduction may severely distort the causal relation, and ESI methods cannot solve it completely. The PDC is an optimized version of DTF, but our study did not demonstrate its advantages in numerical simulation or simultaneous EEG analysis. The EEC achieved a better estimation than DTF ($p = 0.02$) and PDC ($p < 0.01$), but it is still lower than the wPLI (Table I and Table II).

Both similarities and differences exist between simultaneous EEG and numerical simulation analysis. The wPLI achieved better performance in both cases. The PCC is good in numerical simulation at the brain regions level but yields poor results in simultaneous EEG analysis.

B. Effect of Inverse Solutions

The sLORETA, wMNE, and LCMV have different mathematical or physical constraints. The wMNE is the solution with minimum power determined [16], LCMV assumes only one dipole at a time [17]. sLORETA is subject to biophysical constraints. The imaged sources by the above methods were compared with the SEEG recordings in the simultaneous EEG analysis. At the voxel level, there is no significant difference

(a) Brain regions

(b) Simulated signals

(c) Voxel
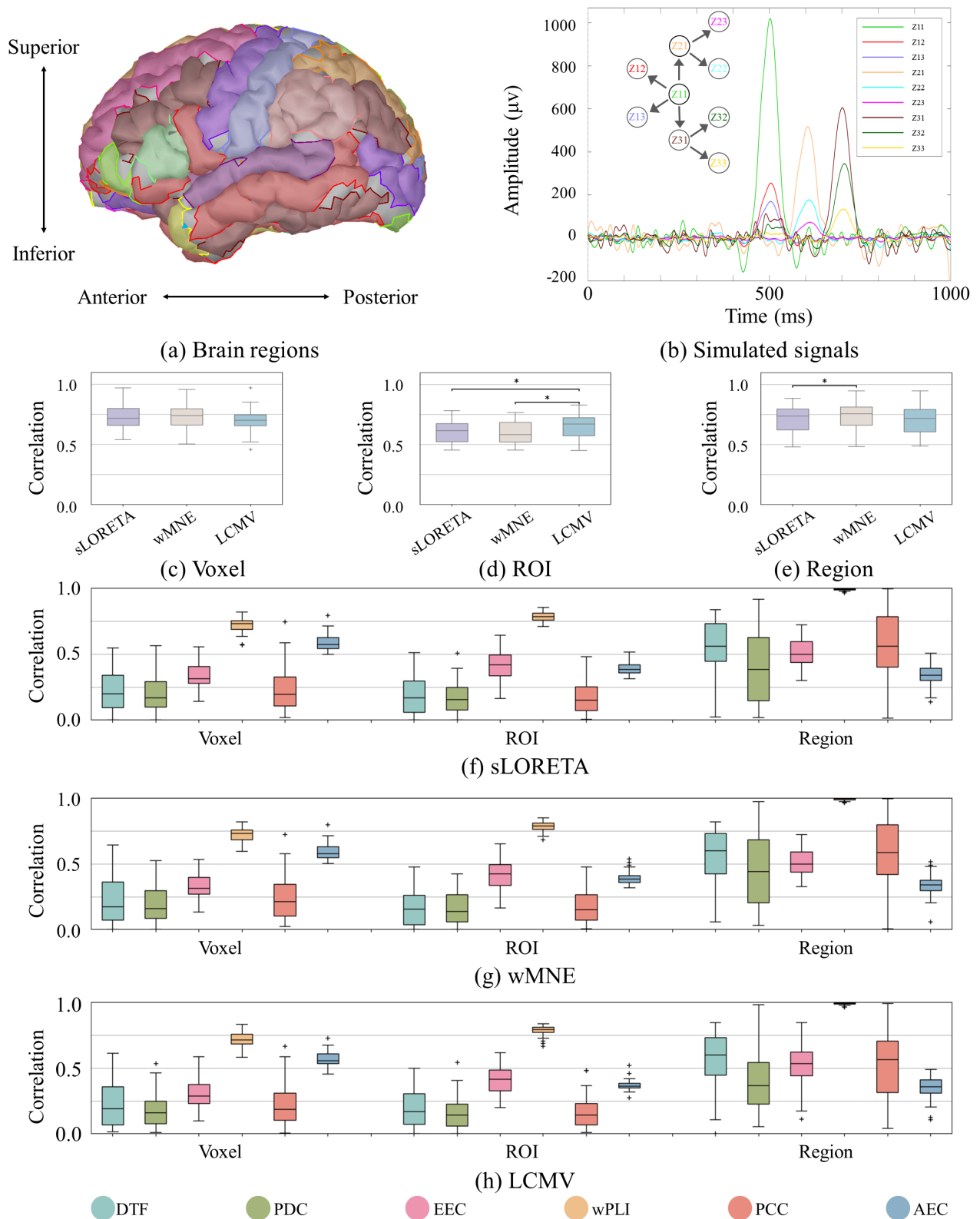
(d) ROI

(e) Region

(f) sLORETA

(g) wMNE

(h) LCMV

Fig. 3. Numerical simulation on the effect of inverse solutions, connectivity measures, and node sizes. (a) Brain regions candidate for nodes. (b) Simulated source signals and connectivity diagram for nine nodes. (c)-(e) Pearson correlation between the source imaging signals and the simulated signals using (c) sLORETA, (d) wMNE, and (e) LCMV, respectively. The * represents a significant difference ($p < 0.01$). (f)-(h) Pearson correlation between the source imaging network and the simulated networks using different network measures with the inverse solution of (f) sLORETA, (g) wMNE, and (h) LCMV, respectively.

between the three ESI methods (Fig. 4(a)), even as the size of the node increased to ROI (Fig. 4(b)) and brain region level (Fig. 4(c)). But in the numerical simulation, we found a significant difference between them (Fig. 3(d) and 3(e)).

	DTF			PDC			EEC			wPLI			PCC			AEC		
	voxels	ROIs	Regions	voxels	ROIs	Regions	voxels	ROIs	Regions	voxels	ROIs	Regions	voxels	ROIs	Regions	voxels	ROIs	Regions
sLORETA	0.20	0.17	0.56	0.17	0.15	0.38	0.31	0.42	0.50	0.73	0.78	0.99	0.19	0.15	0.56	0.57	0.38	0.34
wMNE	0.17	0.15	0.60	0.16	0.14	0.44	0.31	0.42	0.50	0.73	0.79	0.99	0.21	0.15	0.58	0.58	0.38	0.34
LCMV	0.19	0.17	0.60	0.16	0.14	0.37	0.29	0.41	0.53	0.71	0.79	0.99	0.19	0.14	0.56	0.55	0.36	0.36

(a) Voxel   (b) ROI   (c) Region
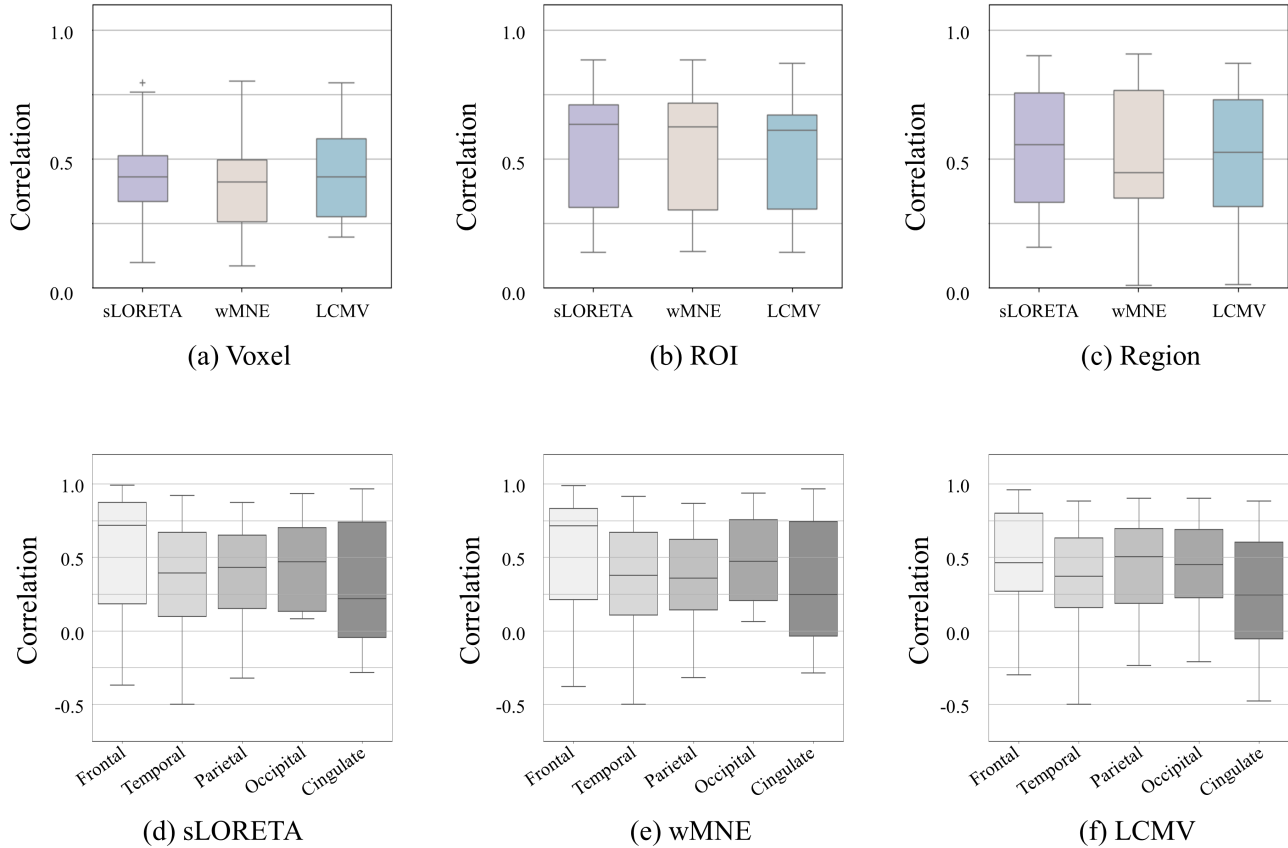
(d) sLORETA   (e) wMNE   (f) LCMV

Fig. 4. Correlation between the imaged sources and SEEG in simultaneous EEG analysis. (a)-(c) Correlation between the SEEG and the imaged sources at (a) voxel, (b) ROI, and (c) region levels. (d)-(f) Correlation between the SEEG and the imaged sources using (d) sLORETA, (e) wMNE, and (f) LCMV in frontal, temporal, parietal, occipital, and cingulate cortex.

	DTF			PDC			EEC			wPLI			PCC			AEC		
	voxels	ROIs	Regions	voxels	ROIs	Regions	voxels	ROIs	Regions	voxels	ROIs	Regions	voxels	ROIs	Regions	voxels	ROIs	Regions
sLORETA	0.38	0.34	0.52	0.14	0.23	0.33	0.35	0.47	0.58	0.71	0.83	0.85	0.20	0.11	0.12	0.67	0.61	0.68
wMNE	0.35	0.42	0.48	0.16	0.23	0.30	0.33	0.46	0.59	0.71	0.83	0.87	0.23	0.11	0.14	0.67	0.61	0.68
LCMV	0.37	0.55	0.50	0.21	0.39	0.45	0.38	0.45	0.56	0.70	0.84	0.88	0.23	0.11	0.12	0.63	0.59	0.64

We think it is mainly due to the simulated clean background activity in the numerical simulation.

When compared at the voxel level, the correlation in the frontal lobe was higher than other lobes for sLORETA (Fig. 3(d)) and wMNE (Fig. 3(e)). When LCMV was used, the correlation in the parietal lobe was higher than that in other lobes. The deep sources in the cingulate cortex scored the lowest correlation in all three inverse methods, which is consistent with other studies [47], [48].

Our results suggest that the ESI measures are essential for analyzing the network using scalp EEG (Fig. 6). In certain cases, wMNE/DTF and sLORETA/PDC, our preliminary results did not show their advantages over the scalp EEG network, and extreme caution should be taken when using them.

C. Effect of Node Sizes

We investigated source signals and source networks at three levels, i.e., voxel, ROI, and brain region. Neuromodulation is an effective solution to treat network diseases. Different neuromodulation methods have targets with different sizes; for example, tDCS affects large brain
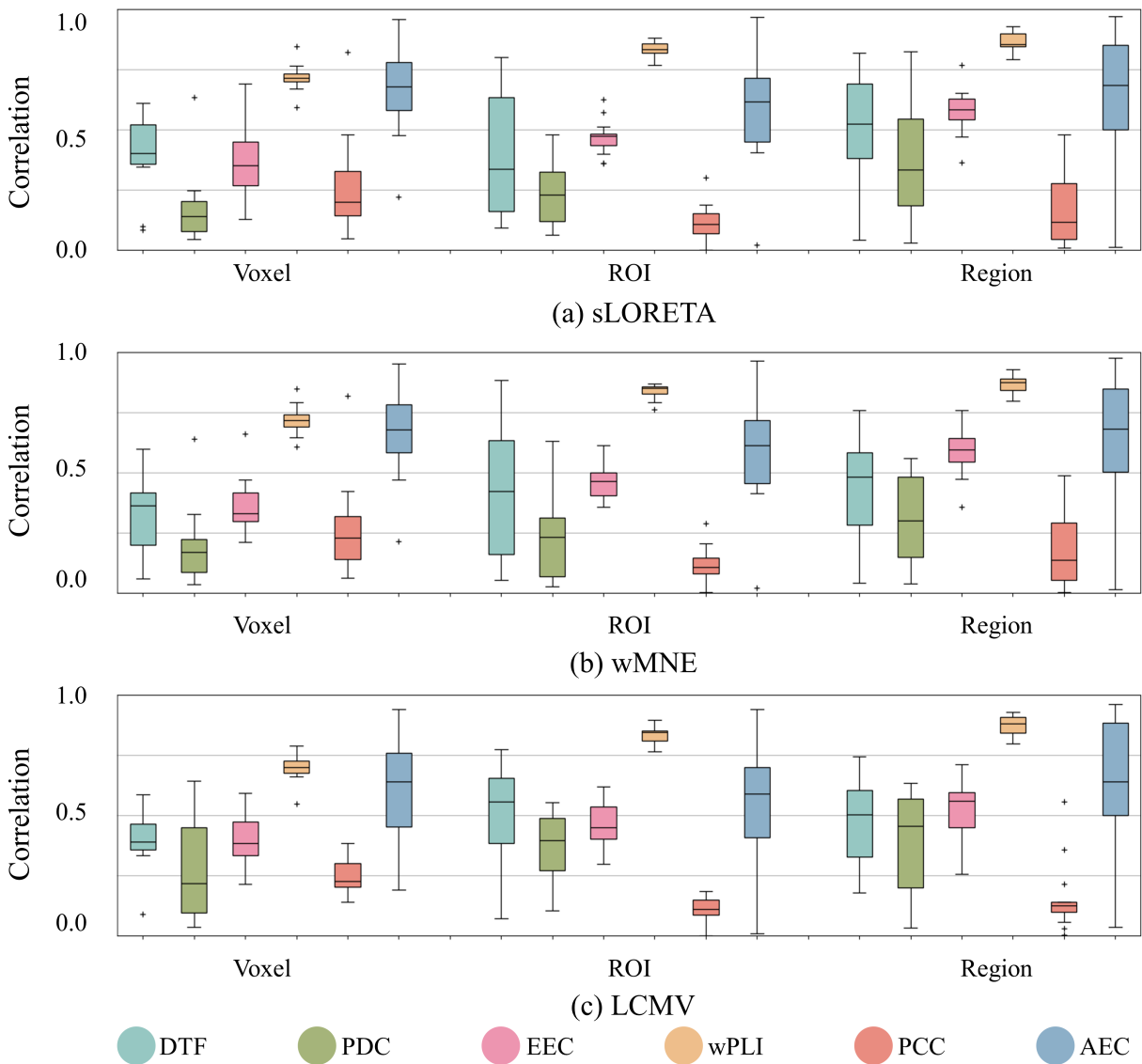
Fig. 5. Pearson correlation using inverse solutions, network measures, and node sizes in simultaneous EEG analysis. (a) Network correlation when sLORETA is used. (b) Network correlation when wMNE is used. (c) Network correlation when LCMV is used.
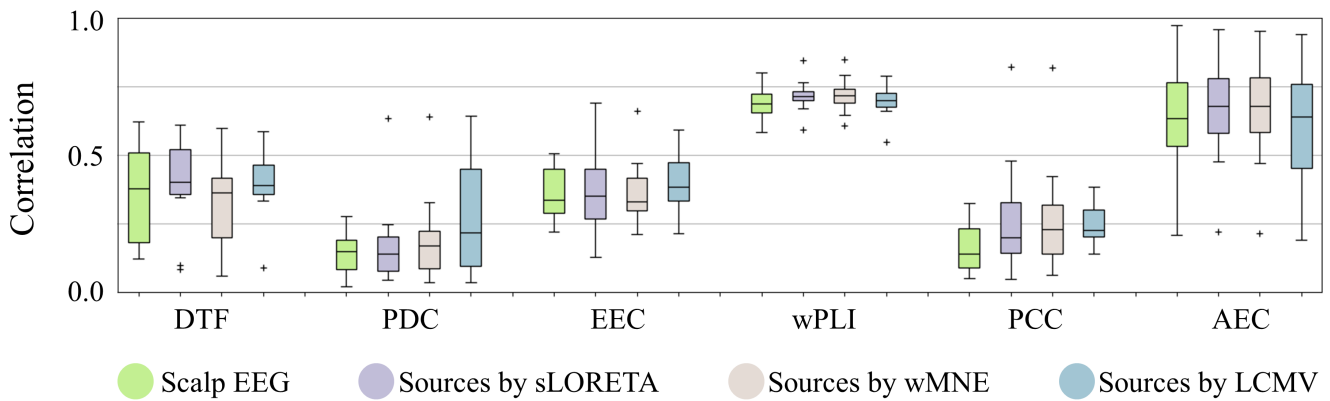

Fig. 6. The correlations between the SEEG network and the network with or without ESI. Pearson correlation between the SEEG network and the scalp EEG network (green boxes) or the source networks by sLORETA, wMNE, and LCMV.

regions, TMS targets ROIs, and tFUS focuses on smaller targets such as a voxel. When ROIs or brain regions are used as the network nodes, LCMV/wPLI is a good choice. When the voxels are used as the network nodes,

the wMNE/wPLI and sLORETA/wPLI are both preferred choices.

D. Limitations

We used evoked simultaneous recording for source imaging studies. The amplitude and rhythm of the evoked signal are stronger than normal brain activity. The connectivity between nodes depends on external stimulation strength and the stimulation site. In addition, we performed superposition averaging processing on the evoked recording, which amplified the prompted information and may reduce some physiological information. The techniques for solving source leakage and extracting connections for brain regions still need further investigation. The use of subcortical signals presents even more significant challenges. The accuracy of the reconstructed signal decreases as the depth increases. So, reconstructing the deep source network is more challenging, which will be addressed in the future study.

V. Conclusion

We explore three factors influencing the source imaging network and study them separately from simulated data and simultaneous EEG. There are no significant differences between the three inverse solutions in the correlation of imaged sources and the SEEG. The wPLI measure provides a more accurate reconstruction of intracranial brain networks than others.

References

[1] M. A. S. Ioana et al., "EEG-based spatiotemporal dynamics of fast ripple networks and hubs in infantile epileptic spasms," *Epilepsia Open*, vol. 9, pp. 1–16, Sep. 2023.

[2] C. Li, A. Sohrabpour, H. Jiang, and B. He, "High-frequency hubs of the ictal cross-frequency coupling network predict surgical outcome in epilepsy patients," *IEEE Trans. Neural Syst. Rehabil. Eng.*, vol. 29, pp. 1290–1299, 2021.

[3] L. Jiang et al., "Spatialrhythmic network as a biomarker of familial risk for psychotic bipolar disorder," *Nat. Mental Health*, vol. 1, pp. 887–899, Oct. 2023.

[4] H. Jiang et al., "Interictal SEEG resting-state connectivity localizes the seizure onset zone and predicts seizure outcome," *Adv. Sci.*, vol. 9, no. 18, Jun. 2022, Art. no. 2200887.

[5] Y. Ren, F. Cong, T. Ristaniemi, Y. Wang, X. Li, and R. Zhang, "Transient seizure onset network for localization of epileptogenic zone: Effective connectivity and graph theory-based analyses of ECoG data in temporal lobe epilepsy," *J. Neurol.*, vol. 266, no. 4, pp. 844–859, Apr. 2019.

[6] P. Qi et al., "EEG functional connectivity predicts individual behavioural impairment during mental fatigue," *IEEE Trans. Neural Syst. Rehabil. Eng.*, vol. 28, no. 9, pp. 2080–2089, Sep. 2020.

[7] T. O. Bergmann, R. Varatheeswaran, C. A. Hanlon, K. H. Madsen, A. Thielscher, and H. R. Siebner, "Concurrent TMS-fMRI for causal network perturbation and proof of target engagement," *NeuroImage*, vol. 237, Aug. 2021, Art. no. 118093.

[8] Y. Hu et al., "Efficacy and safety of simultaneous rTMS–tDCS over bilateral angular gyrus on neuropsychiatric symptoms in patients with moderate Alzheimer's disease: A prospective, randomized, sham-controlled pilot study," *Brain Stimulation*, vol. 15, no. 6, pp. 1530–1537, Nov. 2022.

[9] K. Yu, C. Liu, X. Niu, and B. He, "Transcranial focused ultrasound neuromodulation of voluntary movement-related cortical activity in humans," *IEEE Trans. Biomed. Eng.*, vol. 68, no. 6, pp. 1923–1931, Jun. 2021.

[10] Y. Liu and C. Li, "Localizing targets for neuromodulation in drug-resistant epilepsy using intracranial EEG and computational model," *Frontiers Physiol.*, vol. 13, p. 2022, Oct. 2022.

[11] P. Ryvlin, S. Rheims, L. J. Hirsch, A. Sokolov, and L. Jehi, "Neuromodulation in epilepsy: State-of-the-art approved therapies," *Lancet Neurol.*, vol. 20, no. 12, pp. 1038–1047, Dec. 2021.

[12] F. Babiloni, C. Babiloni, L. Locche, F. Cincotti, P. M. Rossini, and F. Carducci, "High-resolution electro-encephalogram: Source estimates of Laplacian-transformed somatosensory-evoked potentials using a realistic subject head model constructed from magnetic resonance images," *Med. Biol. Eng. Comput.*, vol. 38, no. 5, pp. 512–519, Sep. 2000.

[13] C. M. Michel and D. Brunet, "EEG source imaging: A practical review of the analysis steps," *Frontiers Neurol.*, vol. 10, Apr. 2019, Art. no. 325.

[14] J. C. Bore et al., "Sparse EEG source localization using LAPPS: Least absolute l-P," *IEEE Trans. Biomed. Eng.*, vol. 66, no. 7, pp. 1927–1939, Jul. 2019.

[15] R. D. Pascual-Marqui, "Standardized low-resolution brain electro-magnetic tomography (sLORETA): Technical details," *Methods Find Exp. Clin. Pharmacol.*, vol. 24, pp. 5–12, Jan. 2002.

[16] M. Fuchs, M. Wagner, T. Köhler, and H.-A. Wischmann, "Linear and nonlinear current density reconstructions," *J. Clin. Neurophysiol.*, vol. 16, no. 3, pp. 267–295, May 1999.

[17] B. D. Van Veen, W. Van Drongelen, M. Yuchtman, and A. Suzuki, "Localization of brain electrical activity via linearly constrained minimum variance spatial filtering," *IEEE Trans. Biomed. Eng.*, vol. 44, no. 9, pp. 867–880, Sep. 1997.

[18] A. Sohrabpour, Z. Cai, S. Ye, B. Brinkmann, G. Worrell, and B. He, "Noninvasive electromagnetic source imaging of spatiotemporally distributed epileptogenic brain sources," *Nature Commun.*, vol. 11, no. 1, pp. 19–46, Apr. 2020.

[19] C. Li et al., "Epileptogenic source imaging using cross-frequency coupled signals from scalp EEG," *IEEE Trans. Biomed. Eng.*, vol. 63, no. 12, pp. 2607–2618, Dec. 2016.

[20] R. K. Chikara et al., "Electromagnetic source imaging predicts surgical outcome in children with focal cortical dysplasia," *Clin. Neurophysiol.*, vol. 153, pp. 88–101, Sep. 2023.

[21] R. Sun, A. Sohrabpour, G. A. Worrell, and B. He, "Deep neural networks constrained by neural mass models improve electrophysiological source imaging of spatiotemporal brain dynamics," *Proc. Nat. Acad. Sci. USA*, vol. 119, no. 31, Aug. 2022, Art. no. e2201128119.

[22] A. Ojeda, K. Kreutz-Delgado, and T. Mullen, "Fast and robust block-sparse Bayesian learning for EEG source imaging," *NeuroImage*, vol. 174, pp. 449–462, Jul. 2018.

[23] G. Huang et al., "Electromagnetic source imaging via a data-synthesis-based convolutional encoder–decoder network," *IEEE Trans. Neural Netw. Learn. Syst.*, vol. 36, no. 6, pp. 1–15, Oct. 2022.

[24] J. M. Palva et al., "Ghost interactions in MEG/EEG source space: A note of caution on inter-areal coupling measures," *NeuroImage*, vol. 173, pp. 632–643, Jun. 2018.

[25] E. Vallarino et al., "Tuning minimum-norm regularization parameters for optimal MEG connectivity estimation," *NeuroImage*, vol. 281, Nov. 2023, Art. no. 120356.

[26] S. Allouch, A. Kabbara, J. Duprez, M. Khalil, J. Modolo, and M. Hassan, "Effect of channel density, inverse solutions and connectivity measures on EEG resting-state networks reconstruction: A simulation study," *NeuroImage*, vol. 271, May 2023, Art. no. 120006.

[27] D. Brkić et al., "The impact of ROI extraction method for MEG connectivity estimation: Practical recommendations for the study of resting state data," *NeuroImage*, vol. 284, Dec. 2023, Art. no. 120424.

[28] A.-S. Hincapié et al., "The impact of MEG source reconstruction method on source-space connectivity estimation: A comparison between minimum-norm solution and beamforming," *NeuroImage*, vol. 156, pp. 29–42, Aug. 2017.

[29] S. Haufe and A. Ewald, "A simulation framework for benchmarking EEG-based brain connectivity estimation methodologies," *Brain Topography*, vol. 32, no. 4, pp. 625–642, Jul. 2019.

[30] S. A. H. Hosseini, A. Sohrabpour, and B. He, "Electromagnetic source imaging using simultaneous scalp EEG and intracranial EEG: An emerging tool for interacting with pathological brain networks," *Clin. Neurophysiol.*, vol. 129, no. 1, pp. 168–187, Jan. 2018.

[31] E. Ternisien, T. Cecchin, S. Colnat-Coulbois, L. G. Maillard, and L. Koessler, "Extracting the invisible: Mesial temporal source detection in simultaneous EEG and SEEG recordings," *Brain Topography*, vol. 36, no. 2, pp. 192–209, Mar. 2023.

[32] A. Barborica et al., "Studying memory processes at different levels with simultaneous depth and surface EEG recordings," *Frontiers Hum. Neurosci.*, vol. 17, Apr. 2023, Art. no. 1154038.

[33] F. Pizzo et al., "Deep brain activities can be detected with magnetoencephalography," *Nature Commun.*, vol. 10, no. 1, p. 971, Feb. 2019.

[34] X. Qin et al., "Evaluation of brain source localization methods based on test-retest reliability with multiple session EEG data," *IEEE Trans. Biomed. Eng.*, vol. 70, no. 7, pp. 2080–2090, Jul. 2023.

[35] T. Nguyen, T. Zhou, T. Potter, L. Zou, and Y. Zhang, "The cortical network of emotion regulation: Insights from advanced EEG-fMRI integration analysis," *IEEE Trans. Med. Imag.*, vol. 38, no. 10, pp. 2423–2433, Oct. 2019.

[36] L. Corona et al., "Non-invasive mapping of epileptogenic networks predicts surgical outcome," *Brain*, vol. 146, no. 5, pp. 1916–1931, May 2023.

[37] S. Parmigiani et al., "Simultaneous stereo-EEG and high-density scalp EEG recordings to study the effects of intracerebral stimulation parameters," *Brain Stimulation*, vol. 15, no. 3, pp. 664–675, May 2022.

[38] F. Tadel, S. Baillet, J. C. Mosher, D. Pantazis, and R. M. Leahy, "Brainstorm: A user-friendly application for MEG/EEG analysis," *Comput. Intell. Neurosci.*, vol. 2011, pp. 1–13, Apr. 2011.

[39] F. Tadel et al., "MEG/EEG group analysis with brainstorm," *Frontiers Neurosci.*, vol. 13, p. 76, Feb. 2019.

[40] D. W. Shattuck and R. M. Leahy, "BrainSuite: An automated cortical surface identification tool," *Med. Image Anal.*, vol. 6, no. 2, pp. 129–142, Jun. 2002.

[41] K. Mahjoory, V. V. Nikulin, L. Botrel, K. Linkenkaer-Hansen, M. M. Fato, and S. Haufe, "Consistency of EEG source localization and connectivity estimates," *NeuroImage*, vol. 152, pp. 590–601, May 2017.

[42] K. T. Dolan and M. L. Spano, "Surrogate for nonlinear time series analysis," *Phys. Rev. E, Stat. Phys. Plasmas Fluids Relat. Interdiscip. Top.*, vol. 64, no. 4, Sep. 2001, Art. no. 046128.

[43] L. A. Baccalá and K. Sameshima, "Partial directed coherence: A new concept in neural structure determination," *Biol. Cybern.*, vol. 84, no. 6, pp. 463–474, May 2001.

[44] D. M. Khan, N. Yahya, N. Kamel, and I. Faye, "A novel method for efficient estimation of brain effective connectivity in EEG," *Comput. Methods Programs Biomed.*, vol. 228, Jan. 2023, Art. no. 107242.

[45] M. Vinck, R. Oostenveld, M. van Wingerden, F. Battaglia, and C. M. A. Pennartz, "An improved index of phase-synchronization for electrophysiological data in the presence of volume-conduction, noise and sample-size bias," *NeuroImage*, vol. 55, no. 4, pp. 1548–1565, Apr. 2011.

[46] S. Allouch et al., "Mean-field modeling of brain-scale dynamics for the evaluation of EEG source-space networks," *Brain Topography*, vol. 35, no. 1, pp. 54–65, Jan. 2022.

[47] M. Seeber, L.-M. Cantonas, M. Hoevels, T. Sesia, V. Visser-Vandewalle, and C. M. Michel, "Subcortical electrophysiological activity is detectable with high-density EEG source imaging," *Nature Commun.*, vol. 10, no. 1, p. 753, Feb. 2019.

[48] K. Unnwongse et al., "Validating EEG source imaging using intracranial electrical stimulation," *Brain Commun.*, vol. 5, no. 1, Feb. 2023, Art. no. fcad023.